This article has been accepted for inclusion in a future issue of this journal. Content is final as presented, with the exception of pagination.

On Extending Signal-to-Noise Ratio of Resonators for a MEMS Resonant Accelerometers Using Nonlinearity Compensation

Chengxin Li, Aojie Quan, Hemin Zhang, Chen Wang, Linlin Wang, Mustafa Mert Torunbalci, *Senior Member, IEEE*, Yuan Wang, *Member, IEEE*, and Michael Kraft, *Member, IEEE*

***Abstract*— In this work, the relationship between nonlinear effects and the signal-to-noise ratio of a resonator is analyzed and the impact of reducing nonlinear effects of the resonator on the performance of a resonant accelerometer is investigated. A theoretical framework is formulated to evaluate the dynamic range of the double clamped-clamped resonator. A reduction of the mechanical nonlinearity is achieved through an external electrostatic force, resulting in an enhancement of the dynamic range from 93.8 dB to 132.6 dB. Experimental findings indicate the nonlinear coefficient is reduced to 2.2% compared to an approach without nonlinearity compensation. The nonlinearity compensation demonstrates a 12.8 dB improvement in the signal-to-noise ratio of the resonator, leading to a 5.5-fold increase in resolution of the accelerometer and an extension of the dynamic range by 15 dB. The proposed technique enables the performance of resonant sensors to be further optimized. [2024-0107]**

***Index Terms*— Signal-to-noise ratio, resonant accelerometer, nonlinear effects, dynamic range, nonlinearity compensation.**

I. Introduction

MICRO-ELECTRICAL-MECHANICAL resonant sensors offer excellent resolution, making them suitable for various applications such as accelerometers [2] and mass sensors [3]. Among these, some metrics of the resonant sensors such as long-term stability and resolution are intimately related to the frequency resolution of the resonator. To improve frequency resolution, the signal-to-noise-ratio (SNR) of the resonator should be maximized as it can be shown that it is correlated with the frequency resolution of the resonator [4]:

$$\frac{\Delta\omega}{\omega_0} \approx \frac{1}{2 \cdot \mathrm{Q} \cdot \mathrm{S_{SNR}}} \tag{1}$$

where $\Delta\omega/\omega_0$ is the frequency resolution that is typically determined by the frequency bias instability, Q is the quality factor; and the SNR is given as: $\mathrm{S_{SNR}} = 10^{\mathrm{S_{DR}}/20}$. The dynamic range (DR) of the resonator ($\mathrm{S_{DR}}$) is determined by the thermal-mechanical noise [5] and the maximum linear amplitude (MLA) [6], [7], which, in turn, is limited by the Amplitude-frequency (A-f) effect [8].

To augment the SNR of the resonator, a possible strategy is to employ a higher driving voltage, thus increasing the MLA of the resonator. However, this approach increases intrinsic A-f effects, which can lead to the frequency response transitioning into the nonlinear Duffing regime [9]. Previous research explored the advantages of operating resonators within this nonlinear regime, elucidating its potential to overcome the limitations of the linear regime for MEMS resonators [9], [10], [11], [12], [13]. Investigation of the frequency stability encompassing hysteresis behavior in the nonlinear regime have been empirically compared in references [14], [15], [16], reporting an enhancements of the SNR of the resonators [17]. However, as a trade-off, the hysteresis behavior in the nonlinear regime can cause a deterioration in long-term stability as the driving voltage increases [18]. Thus, increasing the driving voltage while addressing the A-f effect of the resonators has emerged as a viable strategy [6], as illustrated in Fig. 1.

In the past decades, researchers investigated various approaches to address the A-f effect. Suppression of the inherent A-f effect was achieved by tailoring the resonator design parameters [6], [20], [21], [22]. Furthermore, a methodology to reduce the A-f effect was developed using nonlinearity compensation schemes [19]. Electrostatic spring softening to counterbalance mechanical hardening effects has shown promise in enhancing the MLA [23], [24], [25]. Also, reducing the A-f effect with nonlinearity compensation schemes for nanoelectromechanical systems resonators was shown to increase the DR [6], [23]. However, improving the MLA of the resonator by nonlinearity compensation does not reduce the noise floor of the resonant sensor. An electrostatic force

Manuscript received 5 June 2024; revised 1 August 2024; accepted 10 August 2024. This work was supported in part by the Einstein Telescope EMR Site & Technology (E-TEST) of Interreg V-A Euregio Meuse-Rhine (V-A EMR) Project EMRI13 and in part by China Scholarship Council (CSC). An earlier version of this paper was presented in part at the 2023 22nd International Conference on Solid-State Sensors, Actuators and Microsystem [1]. Subject Editor H. Chang. *(Corresponding authors: Hemin Zhang; Chen Wang.)*

Chengxin Li, Aojie Quan, Chen Wang, Linlin Wang, and Michael Kraft are with the Department of Electrical Engineering, ESAT Research Division Micro- and Nano-Systems (ESAT-MNS), 3001 Leuven, Belgium (e-mail: zhanghm@nwpu.edu.cn; chen.wang@esat.kuleuven.be).

Hemin Zhang is with the MOE Key Laboratory of Micro and Nano Systems for Aerospace, Northwestern Polytechnical University, Xi'an 710072, China.

Mustafa Mert Torunbalci was with Broadcom, San Jose, CA 95134 USA. He is now with Google, Goleta, CA 93131 USA.

Yuan Wang is with the Institute of Microelectronics, University of Macau, Macau, China.

Color versions of one or more figures in this article are available at https://doi.org/10.1109/JMEMS.2024.3443641.

Digital Object Identifier 10.1109/JMEMS.2024.3443641

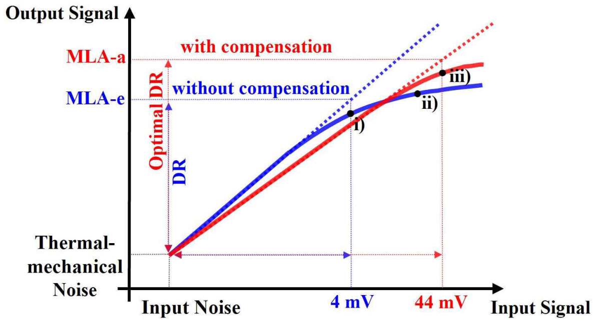

Fig. 1. Comparative illustration of the dynamic range without and with nonlinearity compensation. The blue and red curves represent the response without and with nonlinearity compensation, respectively. MLA-a and MLA-e correspond to the output amplitude of the resonator for input amplitudes of 4 mV and 44 mV, respectively, as discussed in Section III-B. The operational points in this study are defined as: i) conventional maximum linear amplitude, ii) nonlinear amplitude, and iii) nonlinear amplitude with compensation.

from any practical voltage source used for spring softening introduces external noise [26], which can increase the noise floor. Therefore, a detailed experimental investigation is required to explore the effectiveness of compensating the A-f effect, its impact on the SNR of the resonator and, in turn, on the performance of resonant sensors.

This paper presents a comparative analysis of the DR for distinct operational points of the resonator as indicated as (i) $\sim$ (iii) in Fig. 1. The measured frequency stabilities of a resonant accelerometer operating at these points with various DR are utilized to determine the SNR of the resonator. The paper is arranged as follows: In Section II a dynamic model of the resonator is developed to predict the nonlinear coefficients of A-f effect and DR in the presence of a compensation voltage. Section III presents a comparative experiment to verify the theoretical analysis and evaluate the improvement of the SNR at the operational points by nonlinearity compensation. In Section IV limitations of the nonlinearity compensation scheme are discussed and conclusions are drawn.

II. Theory

To demonstrate the influence of nonlinearity compensation on the SNR of the resonator, a resonant accelerometer is utilized in the work. A schematic of the accelerometer is shown in Fig. 2(a). The motion of the proof mass is converted into differential axial forces applied to two resonators through amplification levers [27]. Disregarding the thermal-mechanical noise from the amplification levers, the resolution of the resonant accelerometer is mainly determined by the SNR of the resonators. This means that the resolution of the accelerometer can be improved by either increasing the MLA or by reducing the thermal-mechanical noise of the resonators. In the following, a nonlinear dynamic model is developed to evaluate the theoretical DR of the resonator; then, a numerical solution is obtained using MATLAB.

A. Nonlinear Dynamic Model

The two resonators of the accelerometer comprise a pair of Clamped-Clamped (C-C) beams, as shown in Fig. 2(b).

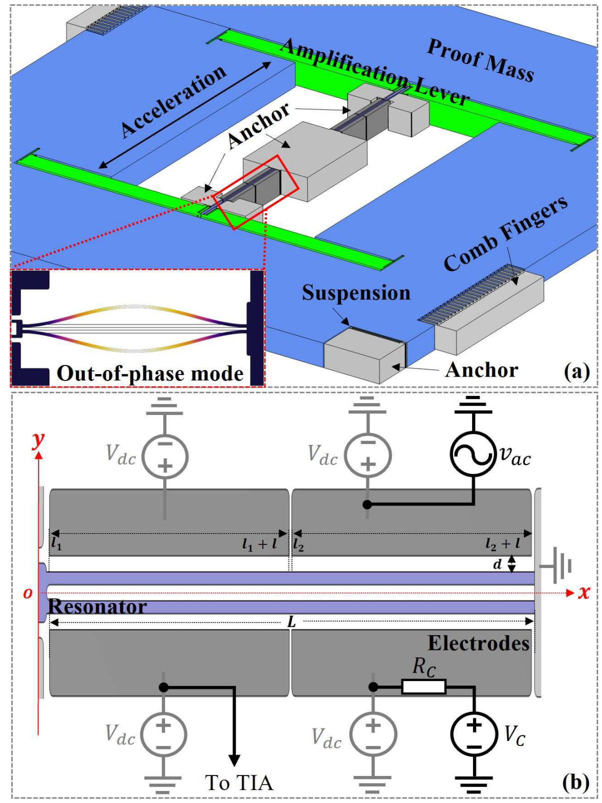

Fig. 2. Schematic of the resonant accelerometer. (b) is the zoom-in schematic with nonlinearity compensation setup in the red-dashed line section of (a). R_C is the intrinsic resistor of the power supply as described in Section III. A.

V_{dc} and v_{ac} are bias and AC drive voltages, respectively. To compensate the nonlinearities of the resonators, an electrostatic nonlinear force is introduced by compensation voltage V_C. Assuming uniformity along the length of the beams, the force dynamics of the C-C beam can be derived in a Cartesian coordinate system using the Bernoulli-Euler equation, yielding:

$$
\begin{aligned}
&EI\frac{\partial^4 w(x,t)}{\partial x^4}+\rho W_e h\frac{\partial^2 w(x,t)}{\partial t^2}+\gamma\frac{\partial w(x,t)}{\partial x}\\
&=\frac{\partial^2 w(x,t)}{\partial x^2}\left(\frac{EW_e h}{2I}\int_0^l\left(\frac{\partial w(x,t)}{\partial x}\right)\right)^2\\
&+\int_{l_2}^{l_2+l}\frac{\varepsilon h\left(V_{dc}+v_{ac}cos(\omega_0 t)\right)^2\phi}{2(d+w(x,t))^2}dx\\
&+\int_{l_2}^{l_2+l}\frac{\varepsilon h\left(V_{dc}+V_C\right)^2\phi}{2(d-w(x,t))^2}dx\\
&+\int_{l_1}^{l_1+l}\frac{\varepsilon h V_{dc}^2\phi}{2(d+w(x,t))^2}dx\\
&+\int_{l_1}^{l_1+l}\frac{\varepsilon h V_{dc}^2\phi}{2(d-w(x,t))^2}dx \qquad (2)
\end{aligned}
$$

where E is Young's modulus, L is the length of the beam, ρ is the density, W_e and h are the width and the thickness of the resonator respectively, d is the air-gap width between the electrodes and the resonator, ε_0 is the permittivity of vacuum, $l_1$and l_2 are the starting positions of the overlap

This article has been accepted for inclusion in a future issue of this journal. Content is final as presented, with the exception of pagination.

areas of the electrodes, and l is the length of the electrodes. $w(x,t)$ is the displacement (in y-axis) of an infinitesimal element of the beam at position x, which is also a function of time t. To solve Eq. (2), the deformation of the elements is separated into a position-dependent mode shape $\phi(x)$ and a time-dependent maximum displacement $u(t)$. Substituting the separated deformation $u(t)\cdot\phi(x)$ and using boundary conditions of $\phi(0)=\phi(L)=0$ [28] into Eq. (2), we obtain:

$$m\frac{\partial^2 u(t)}{\partial t^2}+\gamma\frac{\partial u(t)}{\partial t}+k_1 u(t)+k_2 u(t)^2+k_3 u(t)^3=F_d \tag{3}$$

where F_d represents the driving force, m denotes the effective mass of the C-C beam resonator, and γ the linear damping coefficient. F_d and m are described by Eqs. (4) and (5), respectively.

$$m=\rho h W_e\int_0^1 \phi(x)^2 dx \tag{4}$$

$$F_d=\int_{\frac{l_2}{L}}^{\frac{l_2+l}{L}}\frac{2\varepsilon W_e h V_{dc} v_{ac} cos(\omega t)\phi(x)}{d^2}dx \tag{5}$$

In Eq. (3), $k_r(r=1,2,3)$ represents the rth-order stiffness of the resonator, which is the sum of the rth-order mechanical stiffness k_{mr} and the rth-order electrostatic stiffness k_{er}. By merging similar terms on the left-hand side of Eq. (2), the mechanical stiffness terms can be expressed as.

$$k_{m1}=\int_0^1\frac{EW_e^3 h}{L^3}\left(\frac{d^2\phi(x)}{dx^2}\right)^2 dx \tag{6}$$

$$k_{m3}=\int_0^1\frac{EW_e h}{L^3}\left(\frac{d\phi(x)}{dx}\right)^2 dx \tag{7}$$

where k_{m2} is ignored as the C-C beam resonator operating in a symmetric out-of-phase mode [23]. Expanding the electrostatic force terms on the right-hand side of Eq. (2) by using a Taylor expansion, the electrostatic stiffness terms k_{er}can be derived. It is noteworthy that the 4th-order electrostatic stiffness term is 10^{-3} times smaller compared to the 1st electrostatic stiffness term assuming $x/d<1/10$. Therefore, only the first three terms ($r=1,2,3$) are considered to reduce the complexity of the model. In the initial state of the C-C beam, there are no axial and harmonic forces. Therefore, (disregarding constant electrostatic force terms), the first 3- order terms of electrostatic stiffness can be derived as:

$$k_{e1}=-\int_{\frac{l_2}{L}}^{\frac{l_2+l}{L}}\frac{\varepsilon h\left[3V_{dc}^2+(V_{dc}+V_C)^2\right]\phi(x)}{d^3}dx \tag{8}$$

$$k_{e2}=-\int_{\frac{l_2}{L}}^{\frac{l_2+l}{L}}\frac{\varepsilon h\left[\frac{3}{2}V_{dc}^2+\frac{3}{2}(V_{dc}+V_C)^2\right]\phi(x)}{d^4}dx \tag{9}$$

$$k_{e3}=-\int_{\frac{l_2}{L}}^{\frac{l_2+l}{L}}\frac{\varepsilon h\left[6V_{dc}^2-2(V_{dc}+V_C)^2\right]\phi(x)}{d^5}dx \tag{10}$$

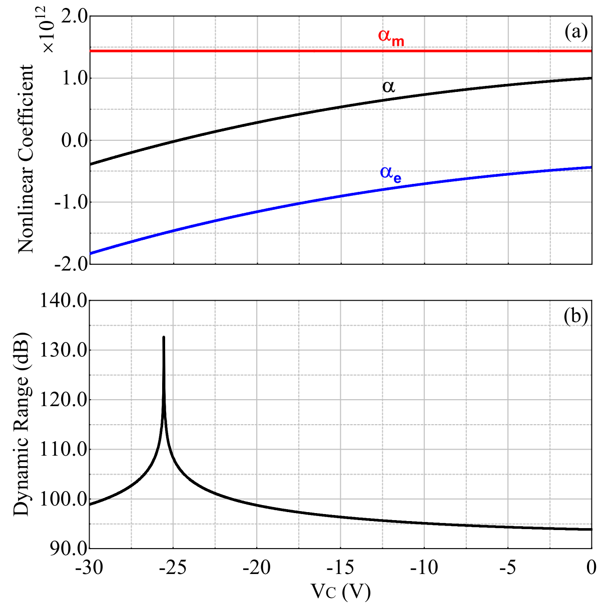

Fig. 3. Numerically calculated (a) nonlinear coefficient and (b) dynamic range as a function of the compensation voltage. The nonlinear coefficient α is the sum of α_m and α_e.

B. Numerical Solution

In this work, the MLA is defined as the point before the onset of nonlinearity [7] and is determined within a 2% linearity error margin with respect to the frequency backbone.

In the resonant accelerometer, the transduction gain of the resonator displacement x depends only on the gain of the Transimpedance Amplifier (TIA) as described in section III-A. Thus, the theoretical DR of the resonator can be calculated by the ratio between the maximum linear displacement of the resonator and the thermal-mechanical displacement due to noise. This thermal-mechanical displacement of the resonator (at the middle of resonator, $x=L/2$) can be expressed as [29]:

$$x_{TN}(\omega)=\frac{\sqrt{4k_B T\left(\frac{\omega_0}{m\mathrm{Q}}\right)}}{\sqrt{\left(\omega^2-\omega_0^2\right)^2+\left(\frac{\omega\omega_0}{\mathrm{Q}}\right)^2}} \tag{11}$$

where k_B is the Boltzmann constant, T is the temperature, ω_0 represents the eigen-frequency of the resonator. Using Eq. (3) and Eq. (11), the theoretical DR of the resonator can be described as Eq. (12).

$$\mathrm{S_{DR}}=20lg\left(\sqrt{\frac{8m\pi^3 f_0^3}{3\sqrt{3}\,k_B T\mathrm{Q}^2}\left|\frac{24k_1^2}{9k_1k_3-10k_2^2}\right|}\right) \tag{12}$$

Following the methodology described in ref [23], we introduce a mechanical (α_m) and an electrostatic nonlinear coefficient (α_e) describing the shift of the frequency peak due to spring hardening or softening, respectively. V_C was swept from 0 V to -30 V in increments of 0.01 V. It can be seen that the total nonlinear coefficient ($\alpha=\alpha_m+\alpha_e$) follows the same trend as α_e whereas α_m remains constant [23]; this is shown in Fig. 3(a).

This article has been accepted for inclusion in a future issue of this journal. Content is final as presented, with the exception of pagination.

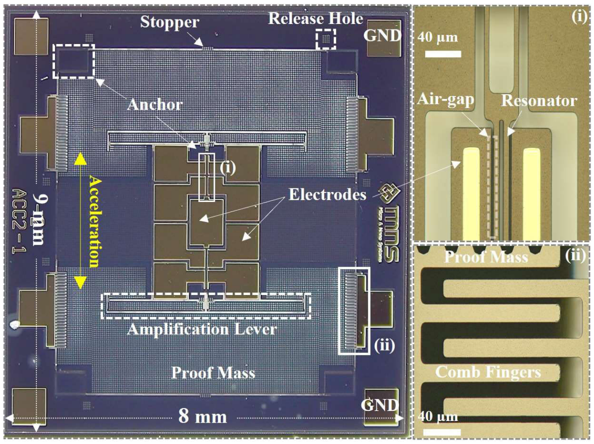

Fig. 4. Micrograph of the resonant accelerometer. (i) and (ii) are close-ups of the resonator and comb fingers used to generate equivalent acceleration, respectively.

TABLE I

KEY PARAMETERS OF THE RESONANT ACCELEROMETER

Parameters	Values
Resonators Area	800×7 μm^2
Suspension Area	550×6.5 μm^2
Amplification Ratio	10
Amplification Lever	2000×20 μm^2
Proof Mass	2.5 mg
Air-gap	3 μm
Thickness	40 μm
Resistivity of Device	0.01 ohm*cm

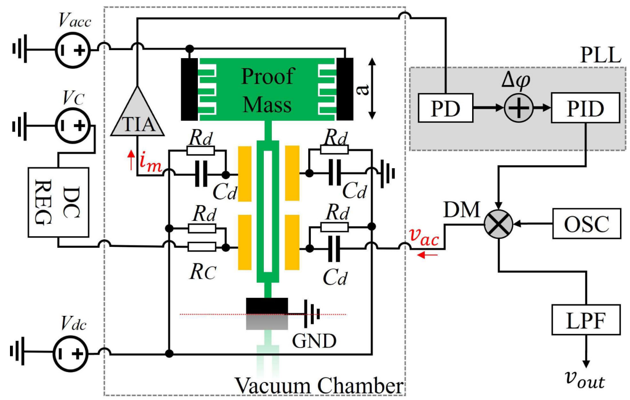

Fig. 5. Schematic of the measurement system showing one half of the setup (the red line is a symmetry line). The TIA provides a gain of 10 MΩ @50 kHz ∼ 250 kHz. DC REG is the DC regulation module. PD is the phase detector, OSC is the digital oscillator, DM is the demodulation module and LPF is the low-pass filter. PLL is the Phase Locked Loop of the lock-in amplifier.

It worth noting that the DR is correlated with 1/Q in Eq. (12). However, the Q factor is also in the denominator of Eq. (1), thus we require a high Q for better resolution of the resonant accelerometer [4]. Therefore, the Q factor was set as the highest value that was achievable in our experimental setup (Q = 10846, section III-A). By substituting Eq. (6) ∼ Eq. (10) into Eq. (12), the numerically calculated results of Eq. (12) are shown in Fig. 3(b). The calculated DR without compensation ($V_C = 0$) is 93.8 dB, whereas the highest DR is 132.6 dB for $V_C = -25.55$ V.

III. EXPERIMENT AND DISCUSSION

A resonant accelerometer based on a double C-C beam, as shown in the micrograph of Fig. 4, was chosen to validate the theoretical predictions and investigate the potential of increasing the SNR of the resonator by minimizing the total nonlinearity. Also, an evaluation of the resonant accelerometer performance (such as: scale factor, bandwidth, resolution) is presented by operating the sensor at the aforementioned operational points with various SNR.

A. Device and Experimental Setup

The device was fabricated using a Silicon-On-Insulator (SOI) wafer with a 40 μm thick device layer, employing a dicing-free process as described in [30]. Stoppers and release holes were used to protect the proof mass during the release process in hydrofluoric (HF) vapor. The size of the accelerometer is 9 mm × 8 mm. The key parameters of the device are listed in Table I.

The experimental setup as shown in Fig. 5 follows the previously described theoretical model. The proof mass and substrate of the accelerometer were grounded to minimize the parasitic capacitance. The mechanical damping constant of the resonator can be adjusted by the applied bias voltage, leading to the bias voltage dependence of the Q factor [31]. Therefore, a bias voltage $V_{dc} = 12$ V was applied at the four electrodes to obtain the highest Q factor according to the experimental observation. A variable compensation voltage V_C was applied using a DC power supply. To address the additional noise caused by fluctuations in the compensation voltage, an active DC regulation module was incorporated into the work. This module consists of a tunable precision voltage reference (REF 102 BU) combined with a low-pass filter (AD8620) and mitigates the primary noise associated with the compensation voltage. The actual noise introduced by the compensation voltage is therefore lower than the noise floor of the circuit. To excite the resonator, an AC voltage v_{ac} was applied using a lock-in amplifier (HFLI Zurich Instrument). For measuring the dynamic response of the resonator, a TIA was used to convert the motional current i_m into an output voltage. Referring to Fig. 5, R_d and C_d are employed to dissipate DC current and to decouple any AC current from the motional current i_m, respectively. The resonant accelerometer and the associated TIA circuitry (A single stage TIA is realized using a commercial operational amplifier (ADA4817-1).) were placed in a vacuum chamber maintained at an ambient pressure of 1 Pa. Furthermore, a DC voltage, denoted as V_{acc}, was applied to the comb fingers to emulate an equivalent acceleration. The proof mass is moved by the electrostatic force exerted by the comb finger and generates an axial force to the resonator through two amplification levers. This yields an equivalent acceleration from −2 g to 2 g.

B. Dynamic Range of the Resonator

For carrying out comparative experiments of the DR of the resonator for different operational modes, the operational

This article has been accepted for inclusion in a future issue of this journal. Content is final as presented, with the exception of pagination.

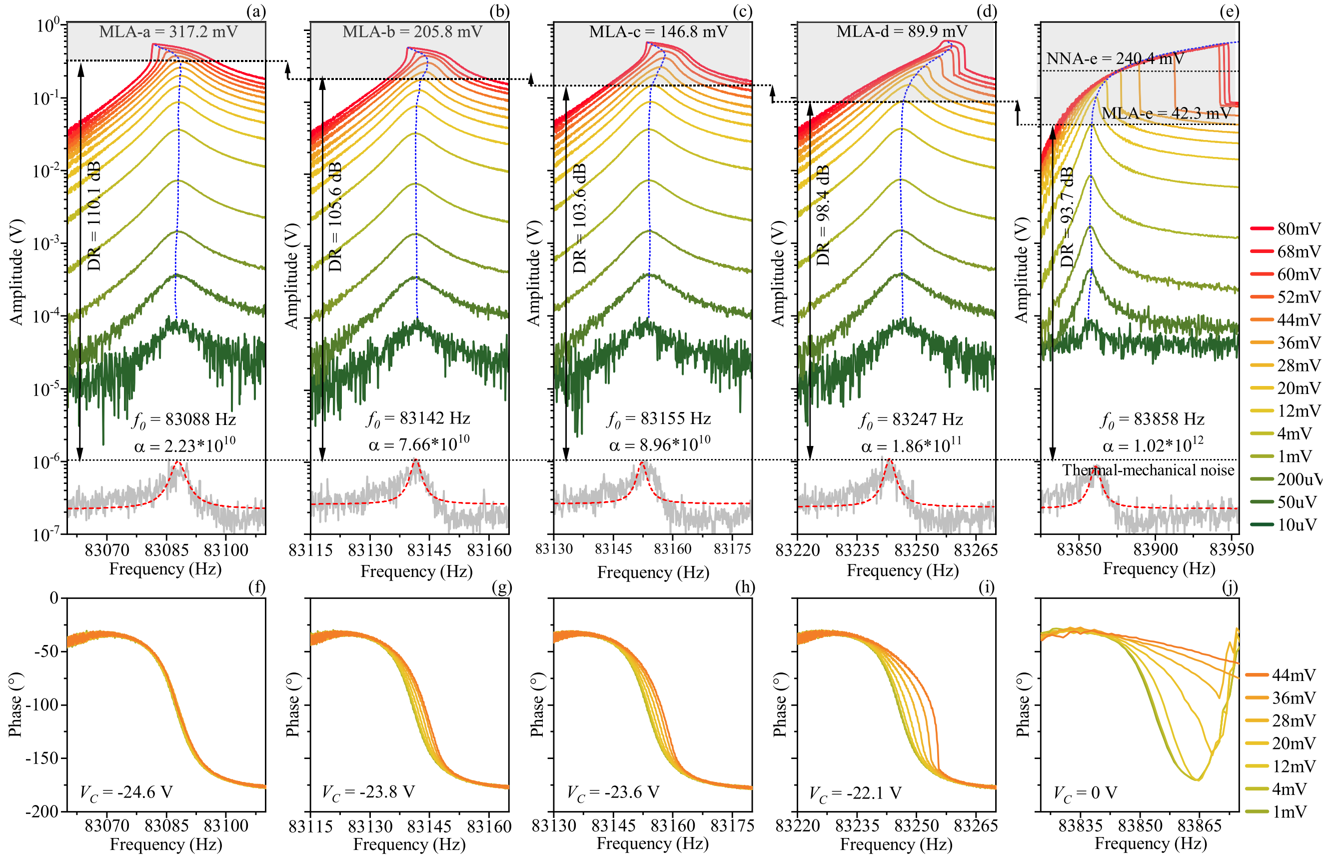

Fig. 6. Measured amplitude-frequency response and phase-frequency response with different compensation voltage. (a) ∼ (e) shows the amplitude-frequency response of the resonator, with compensation voltages V_C of (a) −24.6 V, (b) −23.8 V, (c) −23.6 V, (d) −22.1 V and (e) 0 V, respectively. (f) ∼ (h) shows the phase-frequency responses of the resonator. Similarly, V_C was set to (f) −24.6 V, (g) −23.8 V, (h) −23.6 V, (i) −22.1 V and (j) 0 V, respectively. The operational point NNA-e is in the mechanical nonlinear regime when v_{ac} is 28 mV.

points (i) ∼ (iii) (Fig. 1) are termed as MLA-e, NNA-e and MLA-a for the subsequent measurements, respectively. Measurements of the resonator amplitudes are shown in Fig. 6. The black lines represent the MLA of the operational points (MLA-a ∼ MLA-e) for v_{ac} set to 44 mV, 28 mV, 20 mV, 12 mV, and 4 mV, respectively.

1) Without Nonlinearity Compensation: As the total nonlinear coefficient α (equal to α_m in this case) is positive without compensation voltage ($V_C = 0$ V), it manifests itself as spring hardening. The maximum linear amplitude is 42.3 mV (using the gain of the TIA) and the DR is 93.7 dB; see Fig. 6(e). The eigen-frequency increases as v_{ac} increases monotonically from 10 μV to 80 mV. The phase-frequency response exhibits a steep variation, as shown in Fig. 6(j). The phase at the eigen-frequency peak (MLA-e) ranges from $-110°$ to $-101°$ as v_{ac} increases uniformly from 1 mV to 44 mV. It is also worth noting that the amplitude of v_{out}, shown as a spectrum density using a Fast-Fourier-Transform (FFT) performed by the Lock-in amplifier, exhibits saturation as v_{ac} increases: this is shown in Fig. 7.

2) With Nonlinearity Compensation: On the contrary, the electrostatic nonlinearity leads to a negative or spring softening effect, since the mechanical nonlinearity effect is compensated by the electrostatic nonlinearity effect. The eigen-frequency of the resonator thus decreases in the nonlinear regime. To be specific, the nonlinear coefficient α at point MLA-a

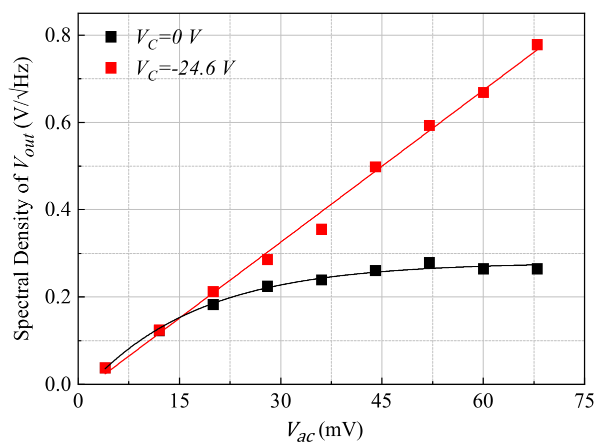

Fig. 7. Measured FFT of the output voltage without V_C and with $V_C = -24.6$ V. The bandwidth of the low-pass filter was 100 Hz.

is approximately 2.2% of point MLA-e. The reduction of the nonlinear coefficient significantly improves the MLA of the resonator. By gradually tuning V_C from −22.1 V to −24.6 V, the measured DR is considerably improved from 93.7 dB to 110.1 dB as depicted in Fig. 6(a). Meanwhile, the thermal-mechanical noise level remains approximately constant. The phase-frequency response exhibits a smooth variation, as shown in Fig. 6(f) to Fig. 6(i). The phase at the

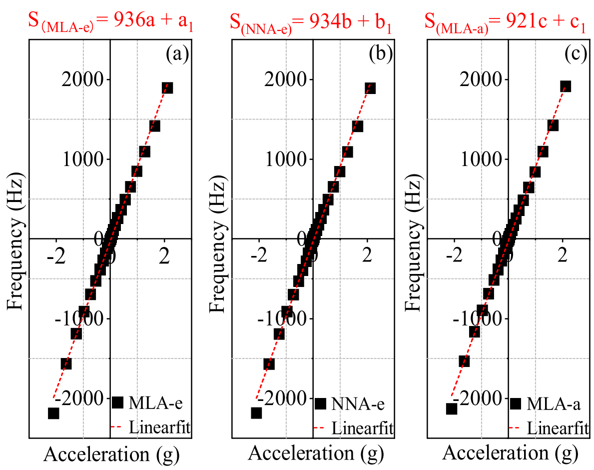

Fig. 8. Measured open-loop static scale factor of the accelerometer based on equivalent acceleration. (a) and (b) are scale factors of MLA-e and NNA-e in Fig 6(e), respectively. (c) is the scale factor of MLA-a with $V_C = -24.6$ V in Fig 6(a).

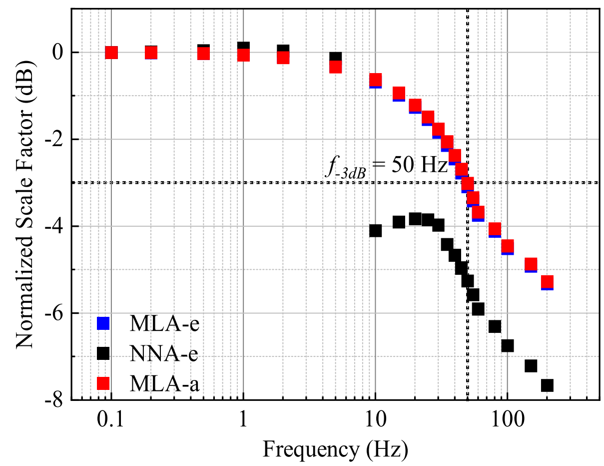

Fig. 9. Measured normalized dynamic scale factor by sweeping the frequency of input acceleration.

eigen-frequency peak (MLA-a) ranges from $-110°$ to $-108°$ as v_{ac} increases uniformly from 1 mV to 44 mV. Typically, such a smooth frequency variation is advantageous for phase control in closed-loop operation. The spectral density of the output signal at the MLA points remains approximately linear with an increase of v_{ac}, as shown in Fig. 7. The white region is considered as the linear operational range whereas the grey region is considered the nonlinear regime.

Although the measured DR follows a similar trend with the compensation voltage, as shown in the theoretical DR from 0 V to -25.55 V in Fig. 3, the measured maximum DR was 110.1 dB which was 22.5 dB lower than the theorectically calculated DR of 132.6 dB. This is attributed to nonideal effects such as fabrications tolerances. Specifically, the fabrication tolerances degrade the symmetry of the resonator due to non-vertical etching profiles and sidewall roughness. This increases the mechanical nonlinear effects of the resonator. Consequently, the measured MLA is lower than the ideal MLA.

C. Scale Factor of the Accelerometer

The open-loop static scale factor of the accelerometer at the different operational points of the resonator was measured by sweeping the voltage to emulate equivalent acceleration from -2 g to 2 g. Without V_C, the measured scale factor of the accelerometer was 936 Hz/g (MLA-e) with a linearity within 2%. In contrast, by operating the accelerometer at MLA-a (for $V_C = -24.6$ V), the negative or spring softening effect leads to a small decrease of 1.5% in the frequency sensitivity of the resonator. In this case, the static scale factor of the accelerometer was 921 Hz/g, as shown in Fig. 8(c).

The dynamic scale factor of the accelerometer is not constant but will change with the frequency of the acceleration, which leads to bandwidth limitations. To obtain the detection limit of the accelerometer, closed-loop measurements are mandatory. The bandwidth of the accelerometer is obtained by taking the -3 dB scale factor drop as the cutoff frequency. In closed-loop configuration, a PLL was used to lock the resonator at different operational points. Then, a square wave signal is applied to the proof mass through the comb fingers to emulate a dynamic acceleration from 0.1 Hz to 200 Hz. As shown in Fig. 9, the dynamic scale factor of the accelerometer operating at point MLA-e exhibits a similar frequency dependency and thus bandwidth compared to point MLA-a (approximately 50 Hz). In sharp contrast, the normalized scale factor drops below 10 Hz when the accelerometer operates at NNA-e. This phenomenon may be attributed to asymmetric oscillations within the mechanical nonlinear regime and needs to be further investigated.

TABLE II
COMPARISON OF THE METRICS ON THE RESONANT ACCELEROMETER

	MLA-e	MLA-a
SNR of Resonator	55.9 dB	68.7 dB
Bandwidth	50 Hz	50 Hz
Sensitivity	936 Hz/g	921 Hz/g
Bias Instability	6.3 μg	1.4 μg
Noise Floor	4.8 μg/√Hz	0.88 μg/√Hz

D. Signal-to-Noise Ratio and Resolution

Similar to the bandwidth measurement, stability measurements of the accelerometer were carried out in closed-loop configuration. An approximation of the SNR of the resonator can be obtained by rearranging Eq. (1):

$$S_{\text{SNR}} \approx \frac{1}{2\text{Q}} \frac{\omega_0}{\Delta\omega} \tag{13}$$

From measurements, $\Delta\omega/\omega_0$ was extracted from the Allan Deviation of the output at 1-second integration time. The Q factor of the resonator was 10846, determined using the ring-down method. Due to a lower frequency stability, the SNR without compensation voltage declines with v_{ac}, as depicted in Fig. 10. A decrease of frequency stability has also been observed in previous work [15]. In contrast, the SNR of point MLA-a shows an increase from 55.9 dB (for v_{ac} 4 mV, resulting in the MLA without compensation voltage), to 68.7 dB for a v_{ac} of 44 mV (resulting in the MLA with V_C =-24.6 V.)

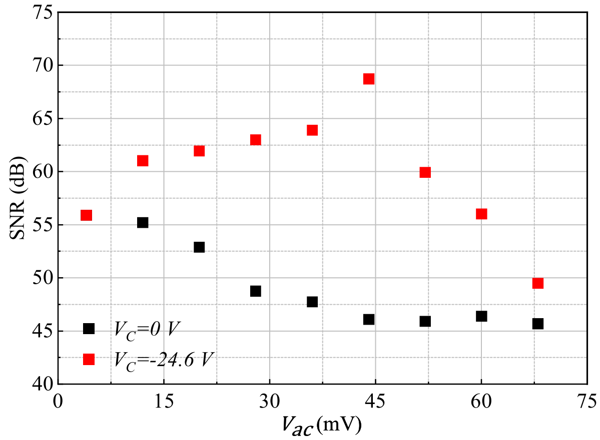

Fig. 10. SNR of the resonator using Eq. (13) based on measured results without V_C and with $V_C = -24.6$ V as a function of v_{ac}.

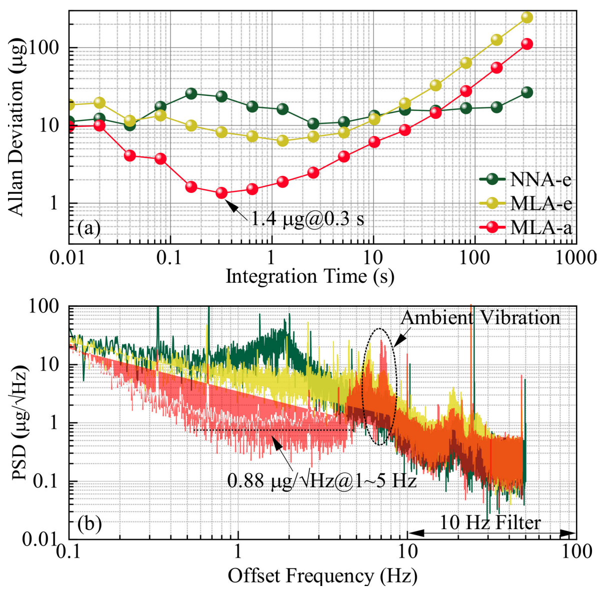

Fig. 11. Measured resolution of the accelerometer in a vacuum environment. (a) Allan Deviation comparison for different operational points. (b) Power Spectrum Density comparison for different operational points.

In principle, the SNR could be further extended by weakening the intrinsic mechanical nonlinear coefficient when $v_{ac} > 44$ mV. However, the SNR shows a steep decline for $v_{ac} > 44$ mV. This is due to the fact that the DR of the resonator is reduced as nonlinear effects reduce the MLA (see Fig. 6(a)) [18]. Within this study, the nonlinearity compensation method introduced by k_{e3} is restricted to levels below 44 mV for v_{ac}. Thus, the threshold for extending SNR using nonlinearity compensation method is delineated within 11-fold v_{ac} without compensation.

The resolution of the accelerometer was measured in a vacuum chamber. Fig. 11 shows the bias instability (derived from the Allan Deviation) and the noise floor for the accelerometer operating at NNA-e, MLA-a and MLA-e; for point MLA-e was 6.4 μg@1.5 s and 4.8 $\mu g/\sqrt{\text{Hz}}$@1 $\sim$ 5 Hz, respectively. Ambient vibrations were inevitable, as evident from the PSD shown in Fig. 11(b). It can be seen that the bias instability and the noise floor of the accelerometer operating at MLA-a were significantly improved. The optimal bias instability was 1.4 μg@0.3 s and the noise floor was 0.88 $\mu g/\sqrt{\text{Hz}}$@1$\sim$5 Hz. Table. II summarizes the main metrics of the accelerometer operating at points MLA-a and MLA-e, respectively.

IV. Conclusion

In conclusion, this work shows that the SNR of the resonator can be enhanced by reducing the A-f effect of the resonator. As a proof of concept, the resolution of a resonant accelerometer is increased by extending the SNR of the resonator without compromising the sensor bandwidth. However, the threshold for SNR extension remains restricted by the inherent Duffing limitation of the resonator [32]. Hence, further research aimed at optimizing the nonlinearity compensation approach will be carried out to increase this threshold.

Acknowledgment

The authors would like to thank Assistant Professor C. Zhao from the University of York for engaging discussions and to Dr. J. Xi from Huazhong University of Science and Technology for her assistance with the theoretical analysis engaging discussions.

References

[1] C. Li et al., "Improving the dynamic range and resolution of MEMS resonant sensors utilizing nonlinear cancellation," in *Proc. 22nd Int. Conf. Solid-State Sensors, Actuat. Microsystems (Transducers)*, 2023, pp. 469–473.

[2] A. A. Seshia et al., "A vacuum packaged surface micromachined resonant accelerometer," *J. Microelectromech. Syst.*, vol. 11, no. 6, pp. 784–793, Dec. 2002.

[3] A. K. Naik, M. S. Hanay, W. K. Hiebert, X. L. Feng, and M. L. Roukes, "Towards single-molecule nanomechanical mass spectrometry," *Nature Nanotechnol.*, vol. 4, no. 7, pp. 445–450, Jul. 2009.

[4] S. K. Roy, V. T. K. Sauer, J. N. Westwood-Bachman, A. Venkatasubramanian, and W. K. Hiebert, "Improving mechanical sensor performance through larger damping," *Science*, vol. 360, no. 6394, Jun. 2018, Art. no. eaar5220.

[5] A. N. Cleland and M. L. Roukes, "Noise processes in nanomechanical resonators," *J. Appl. Phys.*, vol. 92, no. 5, pp. 2758–2769, Sep. 2002.

[6] N. Kacem, J. Arcamone, F. Perez-Murano, and S. Hentz, "Dynamic range enhancement of nonlinear nanomechanical resonant cantilevers for highly sensitive NEMS gas/mass sensor applications," *J. Micromech. Microeng.*, vol. 20, no. 4, Apr. 2010, Art. no. 045023.

[7] Z. Wang and P. X. L. Feng, "Dynamic range of atomically thin vibrating nanomechanical resonators," *Appl. Phys. Lett.*, vol. 104, Mar. 2014, Art. no. 103109.

[8] M. Agarwal et al., "Scaling of amplitude-frequency-dependence nonlinearities in electrostatically transduced microresonators," *J. Appl. Phys.*, vol. 102, no. 7, Oct. 2007, Art. no. 074903.

[9] L. G. Villanueva et al., "Surpassing fundamental limits of oscillators using nonlinear resonators," *Phys. Rev. Lett.*, vol. 110, no. 17, Apr. 2013, Art. no. 177208.

[10] M. Agarwal et al., "Nonlinear characterization of electrostatic MEMS resonators," in *Proc. IEEE Int. Freq. Control Symp. Expo.*, Jun. 2006, pp. 209–212.

[11] H. K. Lee, R. Melamud, S. Chandorkar, J. Salvia, S. Yoneoka, and T. W. Kenny, "Stable operation of MEMS oscillators far above the critical vibration amplitude in the nonlinear regime," *J. Microelectromech. Syst.*, vol. 20, no. 6, pp. 1228–1230, Dec. 2011.

[12] N. Kacem and S. Hentz, "Bifurcation topology tuning of a mixed behavior in nonlinear micromechanical resonators," *Appl. Phys. Lett.*, vol. 95, no. 18, Nov. 2009, Art. no. 183104.

[13] M. Agarwal et al., "Non-linearity cancellation in MEMS resonators for improved power-handling," in *IEDM Tech. Dig.*, Dec. 2005, pp. 286–289.

[14] D. Antonio, D. H. Zanette, and D. López, "Frequency stabilization in nonlinear micromechanical oscillators," *Nature Commun.*, vol. 3, no. 1, p. 806, May 2012.

[15] G. Sobreviela et al., "Parametric noise reduction in a high-order nonlinear MEMS resonator utilizing its bifurcation points," *J. Microelectromech. Syst.*, vol. 26, no. 6, pp. 1189–1195, Dec. 2017.

[16] L. Huang, S. M. Soskin, I. A. Khovanov, R. Mannella, K. Ninios, and H. B. Chan, "Frequency stabilization and noise-induced spectral narrowing in resonators with zero dispersion," *Nature Commun.*, vol. 10, no. 1, p. 3930, Sep. 2019.

[17] D. K. Agrawal and A. A. Seshia, "An analytical formulation for phase noise in MEMS oscillators," *IEEE Trans. Ultrason., Ferroelectr., Freq. Control*, vol. 61, no. 12, pp. 1938–1952, Dec. 2014.

[18] T. Manzaneque, M. K. Ghatkesar, F. Alijani, M. Xu, R. A. Norte, and P. G. Steeneken, "Resolution limits of resonant sensors," *Phys. Rev. Appl.*, vol. 19, no. 5, May 2023, Art. no. 054074.

[19] A. M. Elshurafa, K. Khirallah, H. H. Tawfik, A. Emira, A. K. S. A. Aziz, and S. M. Sedky, "Nonlinear dynamics of spring softening and hardening in folded-MEMS comb drive resonators," *J. Microelectromech. Syst.*, vol. 20, no. 4, pp. 943–958, Aug. 2011.

[20] D. Chen, Y. Wang, Y. Guan, X. Chen, X. Liu, and J. Xie, "Methods for nonlinearities reduction in micromechanical beams resonators," *J. Microelectromech. Syst.*, vol. 27, no. 5, pp. 764–773, Oct. 2018.

[21] J. M. L. Miller et al., "Effective quality factor tuning mechanisms in micromechanical resonators," *Appl. Phys. Rev.*, vol. 5, no. 4, Dec. 2018, Art. no. 041307.

[22] C. Samanta, N. Arora, and A. K. Naik, "Tuning of geometric nonlinearity in ultrathin nanoelectromechanical systems," *Appl. Phys. Lett.*, vol. 113, no. 11, Sep. 2018, Art. no. 113101.

[23] L. C. Shao, M. Palaniapan, and W. W. Tan, "The nonlinearity cancellation phenomenon in micromechanical resonators," *J. Micromech. Microeng.*, vol. 18, no. 6, Jun. 2008, Art. no. 065014.

[24] I. Kozinsky, H. W. C. Postma, I. Bargatin, and M. L. Roukes, "Tuning nonlinearity, dynamic range, and frequency of nanomechanical resonators," *Appl. Phys. Lett.*, vol. 88, no. 25, Jun. 2006, Art. no. 253101.

[25] G. Sobreviela, G. Vidal-Álvarez, M. Riverola, A. Uranga, F. Torres, and N. Barniol, "Suppression of the A-f-mediated noise at the top bifurcation point in a MEMS resonator with both hardening and softening hysteretic cycles," *Sens. Actuators A, Phys.*, vol. 256, pp. 59–65, Apr. 2017.

[26] V. Kaajakari, J. K. Koskinen, and T. Mattila, "Phase noise in capacitively coupled micromechanical oscillators," *IEEE Trans. Ultrason., Ferroelectr., Freq. Control*, vol. 52, no. 12, pp. 2322–2331, Dec. 2005.

[27] Z. Zhang, H. Zhang, Y. Hao, and H. Chang, "A review on MEMS silicon resonant accelerometers," *J. Microelectromech. Syst.*, early access, Jan. 26, 2024, doi: 10.1109/JMEMS.2024.3354235.

[28] C. Li et al., "On enhancing the sensitivity of resonant thermometers based on parametric modulation," *J. Microelectromech. Syst.*, vol. 30, no. 4, pp. 539–549, Aug. 2021.

[29] J. M. L. Miller et al., "Thermomechanical-noise-limited capacitive transduction of encapsulated MEM resonators," *J. Microelectromech. Syst.*, vol. 28, no. 6, pp. 965–976, Dec. 2019.

[30] I. Sari, I. Zeimpekis, and M. Kraft, "A dicing free SOI process for MEMS devices," *Microelectronic Eng.*, vol. 95, pp. 121–129, Jul. 2012.

[31] J. Rieger, T. Faust, M. Seitner, J. Kotthaus, and E. Weig, "Frequency and Q factor control of nanomechanical resonators," *Appl. Phys. Lett.*, vol. 101, no. 10, 2012, Art. no. 103110.

[32] N. Kacem, S. Hentz, D. Pinto, B. Reig, and V. Nguyen, "Nonlinear dynamics of nanomechanical beam resonators: Improving the performance of NEMS-based sensors," *Nanotechnology*, vol. 20, no. 27, Jul. 2009, Art. no. 275501.

Chengxin Li received the M.Sc. degree in precision measurement physics from Huazhong University of Science and Technology, Wuhan, China, in 2021. He is currently pursuing the Ph.D. degree with the Department of Electrical Engineering (ESAT-MNS), KU Leuven, Leuven, Belgium. His current research interests include integrated MEMS resonant accelerometers and device-level vacuum packaging and MEMS resonators.

Aojie Quan received the M.Sc. degree in physics from Shenzhen University, China, in 2018. He is currently pursuing the Ph.D. degree in coupled resonator design and fabrication for sensing application with the University of Leuven. In 2019, he joined the MICAS Laboratories, University of Leuven. His research interests include surface acoustic wave sensors and MEMS coupled resonators.

Hemin Zhang received the B.E. degree in electrical engineering and the Ph.D. degree in microelectromechanical systems and nanotechnology from Northwestern Polytechnical University, Xi'an, China, in 2011 and 2017, respectively. He is currently a Professor with Northwestern Polytechnical University. He has been a Post-Doctoral Researcher with ESIEE Paris, University of Cambridge, Cambridge, and KU Leuven, between 2019 and 2022. His research interests include microelectromechanical systems (MEMS) resonators, coupled resonators, mode-localized sensors, and their conditioning circuitry. He was a recipient of the Outstanding Paper Award Finalist at Transducers in 2015, the Outstanding Paper Award Winner at IEEE MEMS in 2016, the Silver Award of Chinese Mechanical Engineering Society (CMES) Hiwin Doctoral Dissertation Award in 2018, and Marie Skłodowska-Curie (MSCA) Individual Fellowship in 2019.

Chen Wang received the B.S. degree in optical information science and technology from Anhui University, China, in 2013, and the Ph.D. degree in measuring and testing technology from Zhejiang University, China, in 2018. He was a Joint Ph.D. Student with Prof. Michael Kraft with the Montefiore Institute, University of Liege, Belgium. He is currently a Post-Doctoral Researcher with the University of Leuven. His research interests include MEMS inertial sensors, electromechanical sigma–delta modulator interface circuits, and pressure sensors.

Linlin Wang was born in Linyi, China. She received the M.S. degree in mechanical design and theory from Northeastern University, China, in 2019. She is currently pursuing the Ph.D. degree in micro-electric engineering with the ESAT Research Division Micro- and Nano-Systems (MNS), KU Leuven. Her research mainly focuses on coupled BAW MEMS disk resonators for mass sensing applications.

Mustafa Mert Torunbalci (Senior Member, IEEE) received the B.S. degree from the Department of Physics Engineering, Ankara University, Ankara, in 2008, and the M.Sc. and Ph.D. degrees from the Department of Micro and Nanotechnology, Middle East Technical University (METU), Ankara, in 2011 and 2015, respectively. His Ph.D. research focused on developing novel wafer-level fabrication and hermetic packaging platforms for MEMS inertial sensors. From 2015 to 2020, he was a Post-Doctoral Researcher with the School of Electrical and Computer Engineering, Purdue University. Then, he was with Microsoft Quantum Purdue as a Quantum Device Researcher, where he contributed to the development and characterization of semiconductor devices and materials for Microsoft's topological qubit program. From 2020 to 2023, he was a Staff Research and Development Hardware Engineer with the Wireless Semiconductor Division (WSD), Broadcom Inc., focusing on the development of piezoelectric acoustic filters for RF front-end (RFFE) modules in smartphones. Currently, he is a Quantum Hardware Researcher with Google Quantum AI, working on the development of scalable superconducting quantum computers. He has received the Best Ph.D. Thesis Award from METU in 2015 and the Trask Innovation Fund Award from Purdue University in 2018. He has served as a technical program committee (TPC) member for several MEMS conferences. Since 2021, he has been an Associate Editor of the IEEE SENSORS JOURNAL.

Yuan Wang (Member, IEEE) received the B.Eng. degree in electronic engineering from the University of Birmingham, Birmingham, U.K., in 2011, the M.Sc. degree in bioelectronics from The University of Edinburgh, Edinburgh, U.K., in 2012, and the Ph.D. degree in microelectromechanical systems (MEMS) from the University of Liege in 2019. He is currently an Assistant Professor with the Institute of Microelectronics, University of Macau. His research interests include MEMS sensors, microresonators, MEMS system modeling, circuit design, and BioMEMS.

Michael Kraft (Member, IEEE) joined the KU Leuven-MICAS Group as a Full Professor in micro- and nanosystems in October 2017. He brings along 20 years' experience in the design, fabrication, and characterization of a wide range of micro- and nanosystems and micro-electro-mechanical systems (MEMS) sensors and devices. He has worked on inertial sensors, intelligent interface circuits and control systems for micro-devices, atom and ion chips, and bio-medical, and biochemical sensors and devices. These topics will also form the framework of his future research, with a strong focus on bio-medical sensors and systems. He has taken over the lead of the clean room and MEMS activities in Leuven Nanocentre from Prof. Puers.